

HyperST: Hierarchical Hyperbolic Learning for Spatial Transcriptomics Prediction

Chen Zhang^{1*} Yilu An^{1*} Ying Chen^{1,2*} Hao Li¹ Xitong Ling³ Lihao Liu²
Junjun He² Yuxiang Lin^{1†} Zihui Wang^{4†} Rongshan Yu^{1†}

¹Xiamen University ²Shanghai AI Laboratory ³Tsinghua University ⁴Peng Cheng Laboratory

Abstract

*Spatial Transcriptomics (ST) merges the benefits of pathology images and gene expression, linking molecular profiles with tissue structure to analyze spot-level function comprehensively. Predicting gene expression from histology images is a cost-effective alternative to expensive ST technologies. However, existing methods mainly focus on spot-level image-to-gene matching but fail to leverage the full hierarchical structure of ST data, especially on the gene expression side, leading to incomplete image-gene alignment. Moreover, a challenge arises from the inherent information asymmetry: gene expression profiles contain more molecular details that may lack salient visual correlates in histological images, demanding a sophisticated representation learning approach to bridge this modality gap. We propose **HyperST**, a framework for ST prediction that learns multi-level image-gene representations by modeling the data’s inherent hierarchy within hyperbolic space, a natural geometric setting for such structures. First, we design a **Multi-Level Representation Extractors** to capture both spot-level and niche-level representations from each modality, providing context-aware information beyond individual spot-level image-gene pairs. Second, a **Hierarchical Hyperbolic Alignment** module is introduced to unify these representations, performing spatial alignment while hierarchically structuring image and gene embeddings. This alignment strategy enriches the image representations with molecular semantics, significantly improving cross-modal prediction. HyperST achieves state-of-the-art performance on four public datasets from different tissues, paving the way for more scalable and accurate spatial transcriptomics prediction.*

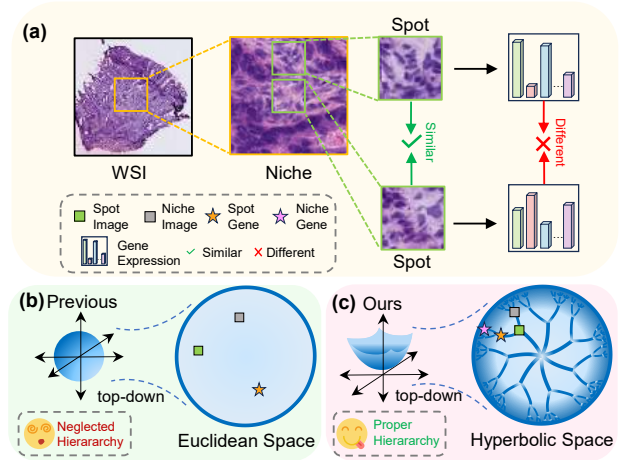


Figure 1. **ST data characteristics.** (a) A WSI contains hierarchical structures and visually similar patterns may correspond to different gene expression profiles. (b) Other works mainly model ST data in Euclidean Space, which neglects niche-level gene and can lead to biased biological insights. (c) Our hyperbolic approach models hierarchies based on information specificity, where a general concept (image/spot) entails its more specific, information-rich counterpart (gene/niche), enabling more informative representation learning.

1. Introduction

Pathological images, particularly Hematoxylin and Eosin (H&E) stained Whole Slide Images (WSIs), provide critical insights into cell morphology and tissue architecture, serving as a cornerstone in biomedical research and clinical diagnosis [4, 7, 24, 27]. Gene expression data complement these pathological images by elucidating the molecular mechanisms underlying observed features, thereby enhancing disease diagnosis and facilitating therapeutic target identification [1]. Spatial Transcriptomics (ST) integrates both modalities by capturing spatially resolved gene expression and cellular morphology simultaneously [38], aligning molecular

*These authors contributed equally to this work.

†Corresponding authors: Yuxiang Lin (linyuxiang@stu.xmu.edu.cn), Zihui Wang (wangzh08@pcl.ac.cn), Rongshan Yu (rsyu@xmu.edu.cn)

profiles with tissue structure at micrometer resolution [44]. Despite its advantages, ST has not achieved widespread clinical adoption due to its high cost and laborious experiment compared to traditional techniques [9, 48]. Consequently, there has been increasing attention on predicting spatially resolved gene expression directly from pathological images using deep learning approaches [42].

Recent studies have explored diverse strategies for this prediction task, including direct inference from spot-level images [16, 30], integration of multi-scale features across WSIs [10, 43], and contrastive learning to align spot-level images with gene expression profiles [46]. Although these methods have shown promising results, several critical questions remain underexplored. Our study is motivated by two key questions in ST prediction: (1) *Can integrating broader pathological and genetic context improve spot-level gene expression inference?* Previous studies often primarily utilized multi-scale pathological features for gene expression prediction, neglecting the multi-level structure inherent in gene expression itself [6, 21], which spans cellular and tissue-level scales. In reality, both broader pathological context and bulk genetic programs can significantly influence the gene expression profile at each spot [5, 32, 45, 47]. (2) *How to encode more molecular information from images under the discrepancy between visual similarity and molecular heterogeneity?* As illustrated in Figure 1 (a), biological heterogeneity may result in visually similar pathology patches exhibiting distinct gene expression patterns [13, 35, 39, 50]. This phenomenon indicates that standard image encoders may fail to capture the subtle morphological cues for predicting these molecular variations. Rather than falling into a one-to-many formulation, we focus on learning a more powerful and molecularly-informed image representation to better capture these complex relationships.

To address these two questions, we introduce **HyperST**, a novel framework for ST prediction by learning multi-level hyperbolic image-gene representations. HyperST tackles these challenges with two core components. First, our **Multi-Level Representation Extractors** capture hierarchical representations from both pathology images and their corresponding gene expression profiles. They extract multimodal information at both spot level and niche level, where a niche consists of a central spot and its surrounding neighbors, enabling the capture of comprehensive morphological and molecular patterns across spatial scales. Second, our **Hierarchical Hyperbolic Alignment** module acts as a powerful structural regularizer rather than a generative model. It uses the unique properties of hyperbolic geometry to impose a meaningful inductive bias on the latent space, guiding the model to learn molecularly-informed features.

We define our hierarchical relationships based on **information specificity**. In this view, a concept A entails a concept B if B is a semantically richer and more specific in-

stance of A. For example, the concept of a “dog on a beach” is more specific and information-rich than “dog”, and is thus considered the child concept. This viewpoint has been adopted in hyperbolic representation learning [11, 15]. Following this principle, we establish two key hierarchies in our framework: (1) A spot-level representation entails its context-rich niche-level counterpart. (2) A morphological image entails its corresponding gene expression. This is because the gene profile contains fine-grained molecular information that offers a much more specific description of the tissue’s state than the more general pathology image. HyperST learns powerful, context-aware representations by modeling information-based hierarchies in hyperbolic space, which is inherently more suited for capturing such structures than Euclidean space [18].

We demonstrate HyperST’s effectiveness on four public datasets from diverse tissues, where it consistently outperforms state-of-the-art models. Our contributions are summarized as:

- We propose **HyperST**, a novel framework for predicting spatially resolved gene expression from WSIs by learning multi-level hyperbolic representations that capture the intrinsic hierarchical structure of ST data.
- We design **Multi-Level Representation Extractors** to capture spot- and niche-level representations from both modalities, providing comprehensive biological insights.
- We introduce **Hierarchical Hyperbolic Alignment** to structurally regularize the latent space, improving cross-modal feature integration.
- Extensive experiments on four public datasets demonstrate that HyperST consistently outperforms existing approaches, underscoring its robust efficacy in spatial gene expression prediction.

2. Related Work

2.1. Prediction of gene expression from images

Recent methodologies for predicting spatially resolved gene expression from histology images have advanced through diverse computational paradigms, including StNet [16], BLEEP [46], TRIPLEX [10], and Stem [50]. Local image-to-expression regression models like StNet employ ResNet50 [17] to directly map H&E image patches to gene expression profiles. While effective in deterministic prediction, these methods assume injective mappings between morphology and transcription, overlooking biological heterogeneity. Multi-scale integration approaches like TRIPLEX extract and fuse multi-resolution features from WSIs using attention mechanisms. Although these methods capture multi-resolution visual patterns, they lack explicit constraints to preserve the essential biological hierarchy. Generative models like Stem address the uncertainty in expression prediction by generating probabilistic gene expression profiles.

While these paradigms better preserve transcriptional variability, they neglect the inherent data hierarchy. In contrast to these prior works, HyperST explicitly models the intrinsic parent-child relationships between spots and their surrounding niches across both imaging and gene expression modalities.

2.2. Multimodal representation learning

Contrastive learning is a pivotal technique for cross-modal tasks by aligning representations across different modalities. For example, CLIP [36] employs contrastive learning to align paired images and texts in a shared Euclidean embedding space. Inspired by CLIP, BLEEP [46] adapts contrastive learning to histology and gene expression, using direct interpolation in the embedding space for efficient, decoder-free predictions. These two models rely on Euclidean embeddings, which limit their ability to capture hierarchical relationships. To overcome these limitations, MERU [11] embeds image and text into hyperbolic space, leveraging its geometric properties to build a hierarchical representation space through contrastive and entailment losses. Building on MERU, HyCoCLIP [34] introduces intra-modal hierarchical modeling by extracting object bounding boxes from images and their corresponding textual descriptions, establishing hierarchical links between box regions and the full image-text pair. HyCoCLIP’s dependence on pre-trained object detection models to derive these boxes from given captions may result in potential inaccuracies. In contrast, HyperST directly leverages the inherent structure of ST data, from spot-level to niche-level contexts, avoiding uncertainties associated with external feature extraction.

3. Method

The overview of HyperST is illustrated in Figure 2. First, we briefly describe the preliminaries of the hyperbolic geometry in Section 3.1. Second, we present the Multi-Level Representation Extractors in Section 3.2. Third, we introduce the Hierarchical Hyperbolic Alignment in Section 3.3. Finally, we describe the Gene Decoder and our Overall Objective Function in Section 3.4.

3.1. Preliminaries

Hyperbolic Geometry Hyperbolic Geometry is a fundamental class of non-Euclidean geometry with a constant negative curvature. This distinguishing characteristic results in an exponential growth of volume with respect to radius, in stark contrast to Euclidean geometry, which exhibits zero curvature and polynomial volume scaling [29]. Consequently, hyperbolic spaces are naturally adept at representing tree-like or hierarchical data structures, where the number of elements increases exponentially with depth [18, 34]. Due to their negative curvature, hyperbolic spaces cannot be isometrically embedded in Euclidean spaces of equivalent dimensional-

ity without compromising distances or angles. To address this issue, several geometric models are employed for their representation and computation, including the Poincaré ball model and the Lorentz model [3, 8].

Lorentz Model Lorentz model is widely preferred due to its numerical stability and straightforward geodesic calculations [31]. The Lorentz model \mathbb{L}_c^n embeds the n -dimensional hyperbolic space as the upper sheet of a two-sheeted hyperboloid in $(n + 1)$ -dimensional Minkowski space, with a constant curvature $-c < 0$. It therefore consists of all vectors satisfying the following conditions:

$$\mathbb{L}_c^n = \{\mathbf{x} \in \mathbb{R}^{n+1} : \langle \mathbf{x}, \mathbf{x} \rangle_{\mathbb{L}} = -\frac{1}{c}, \\ x_{time} = \sqrt{1/c + \|\mathbf{x}_{space}\|^2}, \quad (1) \\ c > 0\},$$

where points $\mathbf{x} \in \mathbb{R}^{n+1}$ in \mathbb{L}_c^n can be represented as $[x_{time}, \mathbf{x}_{space}]$. $x_{time} \in \mathbb{R}$ and $\mathbf{x}_{space} \in \mathbb{R}^n$ denote the *time component* and the *spatial component* [11], respectively. For two vectors $\mathbf{x}, \mathbf{y} \in \mathbb{L}_c^n$, the Lorentzian inner product $\langle \cdot, \cdot \rangle_{\mathbb{L}}$ is defined as $\langle \mathbf{x}, \mathbf{y} \rangle_{\mathbb{L}} = \langle \mathbf{x}_{space}, \mathbf{y}_{space} \rangle_{\mathbb{E}} - x_{time}y_{time}$, where $\langle \mathbf{x}, \mathbf{y} \rangle_{\mathbb{E}}$ represents the Euclidean inner product in \mathbb{R}^n . Besides, the Lorentzian distance $d_{\mathbb{L}}(\mathbf{x}, \mathbf{y})$ measures the length of the shortest path between two points \mathbf{x} and \mathbf{y} , which is formulated as:

$$d_{\mathbb{L}}(\mathbf{x}, \mathbf{y}) = \sqrt{1/c} \cdot \cosh^{-1}(-c\langle \mathbf{x}, \mathbf{y} \rangle_{\mathbb{L}}). \quad (2)$$

Tangent Space and Exponential Map The tangent space of $\mathbf{x} \in \mathbb{L}_c^n$ is denoted by $\mathcal{T}_{\mathbf{x}}\mathbb{L}_c^n$, which is precisely defined as the set of vectors orthogonal to \mathbf{x} under the Lorentzian inner product:

$$\mathcal{T}_{\mathbf{x}}\mathbb{L}_c^n = \{\mathbf{v} \in \mathbb{R}^{n+1} : \langle \mathbf{x}, \mathbf{v} \rangle_{\mathbb{L}} = 0\}. \quad (3)$$

A fundamental mechanism for connecting the tangent space to the hyperbolic manifold is the exponential map. The exponential map $\exp_{\mathbf{x}}^c : \mathcal{T}_{\mathbf{x}}\mathbb{L}_c^n \rightarrow \mathbb{L}_c^n$ projects tangent vector \mathbf{v} onto the \mathbb{L}_c^n along a geodesic emanating from \mathbf{x} in the direction of \mathbf{v} , given by:

$$\exp_{\mathbf{x}}^c(\mathbf{v}) = \cosh(\sqrt{c}\|\mathbf{v}\|_{\mathbb{L}})\mathbf{x} + \frac{\sinh(\sqrt{c}\|\mathbf{v}\|_{\mathbb{L}})}{\sqrt{c}\|\mathbf{v}\|_{\mathbb{L}}}\mathbf{v}, \quad (4)$$

where $\|\mathbf{v}\|_{\mathbb{L}} = \sqrt{\langle \mathbf{v}, \mathbf{v} \rangle_{\mathbb{L}}}$ is the Lorentzian norm. Moreover, the exponential map serves as a bridge between Euclidean and hyperbolic geometries. By interpreting Euclidean vectors as tangent vectors at the origin $\mathbf{O} = [\sqrt{1/c}, 0, \dots, 0] \in \mathbb{R}^{n+1}$ of the hyperbolic space [22, 29, 34], we begin by extending the Euclidean embedding $\mathbf{v}_{euc} \in \mathbb{R}^n$ into \mathbb{R}^{n+1} by defining a vector $\mathbf{v} = [0, \mathbf{v}_{euc}] \in \mathbb{R}^{n+1}$. This vector \mathbf{v} is

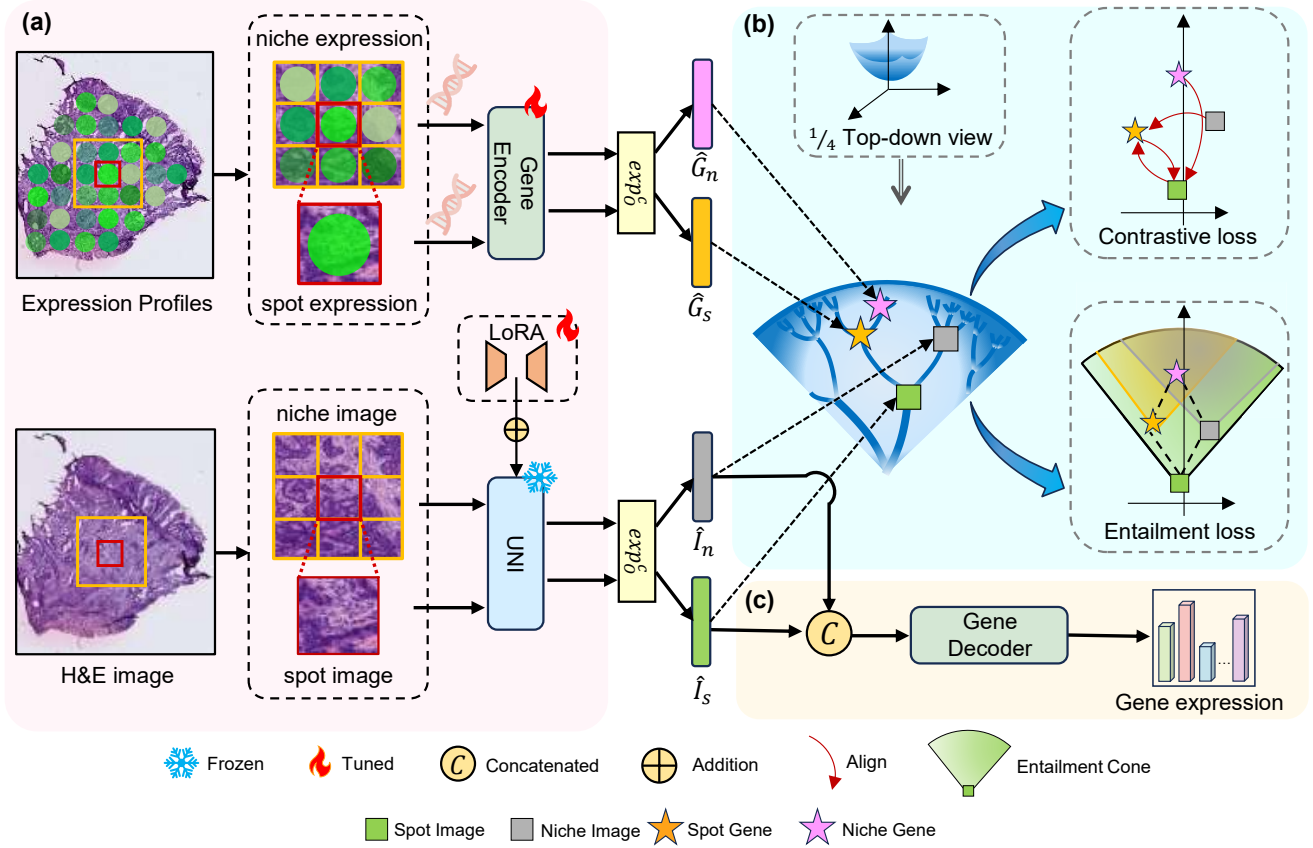


Figure 2. **Overview of HyperST.** HyperST consists of three components. (a) **Multi-Level Representation Extractors** capture spot- and niche-level features from both images and gene expression. (b) **Hierarchical Hyperbolic Alignment** module projects these features into a shared hyperbolic latent space. It uses contrastive alignment for corresponding image-gene pairs and entailment alignment to structurally regularize the latent space according to information hierarchies. (c) **Gene Decoder** uses the resulting aligned and context-aware image representations to predict spot-level gene expression.

situated in the tangent space at the origin \mathbf{O} of the hyperboloid as $\langle \mathbf{O}, \mathbf{v} \rangle_{\mathbb{L}} = 0$. Thus, \mathbf{v} can be projected onto the hyperboloid \mathbb{L}_c^n employing the exponential map:

$$\mathbf{x}_{space} = \exp_{\mathbf{O}}^c(\mathbf{v}_{euc}) = \frac{\sinh(\sqrt{c}\|\mathbf{v}_{euc}\|_{\mathbb{E}})}{\sqrt{c}\|\mathbf{v}_{euc}\|_{\mathbb{E}}} \mathbf{v}_{euc}. \quad (5)$$

Then we can directly calculate the corresponding time component x_{time} from \mathbf{x}_{space} . The detailed derivations of the above equations can be found in Section 6 of the Supplementary Material.

Hyperbolic Entailment Loss The entailment cone $\mathcal{R}_{\mathbf{y}}$ constitutes a region around the point \mathbf{y} where all points $\mathbf{x} \in \mathcal{R}_{\mathbf{y}}$ represent child concepts of the parent concept \mathbf{y} [11, 14], defined by the half-aperture:

$$\text{aper}(\mathbf{y}) = \sin^{-1} \left(\frac{2K}{\sqrt{c}\|\mathbf{y}_{space}\|} \right), \quad (6)$$

where $K = 0.1$ determines boundary conditions near the origin. To enforce the partial order relationship where \mathbf{y} entails \mathbf{x} , the penalty is formulated as:

$$\mathcal{L}_{entail}(\mathbf{y}, \mathbf{x}) = \max(0, \text{ext}(\mathbf{y}, \mathbf{x}) - \text{aper}(\mathbf{y})), \quad (7)$$

where $\text{ext}(\mathbf{y}, \mathbf{x})$ denotes the exterior angle defined as $\text{ext}(\mathbf{y}, \mathbf{x}) = \cos^{-1} \left(\frac{x_{time} + y_{time} c(\mathbf{y}, \mathbf{x})_{\mathbb{L}}}{\|\mathbf{y}_{space}\| \sqrt{(c(\mathbf{y}, \mathbf{x})_{\mathbb{L}})^2 - 1}} \right)$.

3.2. Multi-Level Representation Extractors

Multi-Level Pathological Images Extractor Following the previous works [46, 50], a spot-level image patch $X_s \in \mathbb{R}^{3 \times L_s \times L_s}$ of each identified spot is extracted and preprocessed from a H&E stained image, with the spot positioned at the center of the patch, as depicted in Figure 2 (a), where L_s represents the size of the spot image. While X_s directly corresponds to the target spot gene expression, the additional nearby visual information from larger-scale pathology patches can significantly contribute to the analy-

sis [10, 26]. Therefore, we introduce the niche-level image patch $X_n \in \mathbb{R}^{3 \times L_n \times L_n}$, which is defined as a higher-level region composed of the central spot-level patch X_s and its spatially adjacent spot-level patches. L_n signifies the patch size of the niche image. These neighboring patches are selected based on spatial proximity using the K-Nearest Neighbors (KNN) algorithm. By cropping the region of these patches, X_n forms a larger image region that provides a broader field of view and enhanced contextual information about the surrounding tissue microenvironment.

We leverage UNI [4], a pathology foundation model pre-trained on large-scale histology images, to extract feature embeddings for spot-level and niche-level image patches. As the original UNI was not well-suited for large-sized niche-level image patches, we resized the images in our dataset and fine-tuned UNI using the Low-Rank Adaptation (LoRA) technique [19], leading to improved multi-level visual representations. Consider a frozen pre-trained weight matrix $W_{origin} \in \mathbb{R}^{d \times d}$, where d denotes the dimension. The updated weight matrix is formulated as $W_{new} = W_{origin} + \Delta W = W_{origin} + BA$, where the update $\Delta W \in \mathbb{R}^{d \times d}$ expressed by the product of two smaller trainable matrices: $B \in \mathbb{R}^{d \times r}$, $A \in \mathbb{R}^{r \times d}$, and the rank $r \ll d$. This approach enables us to adapt the model to the characteristics of our data while substantially reducing the computational resources required for fine-tuning. The multi-level image representations $I_s \in \mathbb{R}^d$ and $I_n \in \mathbb{R}^d$ are extracted by $I_s, I_n = MIE(X_s, X_n; \theta_{UNI}, \Delta\theta_{lora})$. Here, MIE represents the UNI model adapted by LoRA, θ_{uni} and $\Delta\theta_{lora}$ denote the frozen parameters of UNI and the trainable parameters of LoRA modules.

Multi-Level Genomic Profiles Extractor Let $Y_s \in \mathbb{R}^N$ be the associated spot-level gene expression profile of the spot-level image X_s , where N is the gene set size. In the same vein as the niche-level image patch, we introduce the niche-level gene expression profile $Y_n \in \mathbb{R}^N = \frac{1}{|S|} \sum_{i \in S} Y_s^i$, where $S = \{Y_s^1, \dots, Y_s^K\}$ denotes the expression profile set of Y_s and its neighbors, $K-1$ is the number of selected neighbors. $G_s, G_n = MGE(Y_s, Y_n; \theta_{gene})$, where MGE denotes the multi-level genomic profiles extractor with trainable parameters implemented by a trainable fully connected network θ_{gene} , $G_s \in \mathbb{R}^d$ and $G_n \in \mathbb{R}^d$ are the spot-level and niche-level gene embeddings, respectively.

3.3. Hierarchical Hyperbolic Alignment

To obtain better representations for facilitating the subsequent tasks, the alignment is a pivotal method which bridges the gap of different modalities [25, 46, 49]. However, common implementations of alignment, such as BLEEP [46], directly minimize distances between items in Euclidean space, which may not be appropriate for hierarchical data like ST. To address this problem, we design a **Hierarchical**

Contrastive Alignment module, which aligns the different modalities at different levels in hyperbolic space. Subsequently, we introduce a **Hierarchical Entailment Alignment** module to regularize the partial order in ST data.

Hierarchical Contrastive Alignment (HCA) Using Equation 5, let $\exp_O^c(\cdot) : \mathbb{R}^d \rightarrow \mathbb{L}_c^d$ map Euclidean features to hyperbolic space with trainable curvature $-c < 0$ and origin O . This yields hyperbolic spatial components $\{\hat{I}_s^{space}, \hat{I}_n^{space}, \hat{G}_s^{space}, \hat{G}_n^{space}\} = \exp_O^c(\{I_s, I_n, G_s, G_n\})$, while the corresponding time components can be calculated by Equation 1. The hyperbolic representations $\hat{I}_s, \hat{I}_n, \hat{G}_s$ and \hat{G}_n are obtained by concatenating spatial components and time components. To align the spot-level image embedding to the spot-level embedding, we employ a modified infoNCE loss [33], in which the cosine similarity is replaced by the Lorentzian distance $d_{\mathbb{L}}(\cdot, \cdot)$ described in Equation 2. The contrastive loss is defined as follows:

$$\mathcal{L}_{align}(\hat{I}_s, \hat{G}_s) = -\frac{1}{B} \sum_{i=1}^B \log \frac{\exp(d_{\mathbb{L}}(\hat{I}_s^i, \hat{G}_s^i)/\tau)}{\sum_{j=1, j \neq i}^B \exp(d_{\mathbb{L}}(\hat{I}_s^i, \hat{G}_s^j)/\tau)}, \quad (8)$$

where B denotes the batch size and τ is the temperature parameter. To better utilize in-batch negatives, we also align spot-level gene to spot-level image embeddings using $\mathcal{L}_{align}(\hat{G}_s, \hat{I}_s)$. Since spot-level features represent more general characteristics, a single spot-level feature may correspond to multiple niche-level features within a batch. To avoid such undesirable negative alignment, we only consider the alignment from niche-level features to spot-level features, i.e., $\mathcal{L}_{align}(\hat{G}_n, \hat{I}_s)$ and $\mathcal{L}_{align}(\hat{I}_n, \hat{G}_s)$. The objective function of Hierarchical Contrastive Alignment can be expressed as:

$$\mathcal{L}_{HCA} = \frac{1}{4} (\mathcal{L}_{align}(\hat{I}_s, \hat{G}_s) + \mathcal{L}_{align}(\hat{G}_s, \hat{I}_s) + \mathcal{L}_{align}(\hat{G}_n, \hat{I}_s) + \mathcal{L}_{align}(\hat{I}_n, \hat{G}_s)). \quad (9)$$

Hierarchical Entailment Alignment (HEA) Beyond spot-niche hierarchies, we account for the non-identical nature of image features and gene features. We recognize that gene features provide finer-grained molecular insights. Thus, we posit that gene features are the child concept of images in hyperbolic space. In our ST data, this hierarchy can be summarized as spot-level features entailing niche-level features, and pathological images entailing their corresponding gene expression profiles. In order to directly constrain this hierarchical structure, we leverage Hyperbolic Entailment Loss $\mathcal{L}_{entail}(\cdot, \cdot)$ described in Equation 7. Therefore, the final objective function of this module is formulated as:

Table 1. Performance comparison on four spatial transcriptomics datasets. Higher values on PCC@10, PCC@50, PCC@200 are better. Lower values on MAE, MSE are better.

Dataset	Model	PCC@10 ↑	PCC@50 ↑	PCC@200 ↑	MSE ↓	MAE ↓
Kidney	TRIPLEX	0.579±0.095	0.485±0.084	0.351±0.066	1.122±0.204	0.855±0.104
	StNet	0.523±0.105	0.435±0.095	0.305±0.064	1.167±0.217	0.847±0.078
	BLEEP	0.518±0.112	0.434±0.102	0.310±0.071	1.233±0.244	0.865±0.085
	Stem	0.535±0.111	0.414±0.084	0.271±0.059	1.380±0.347	0.911±0.115
	HyperST	0.617±0.094	0.526±0.088	0.390±0.070	1.077±0.155	0.817±0.058
Colorectum	TRIPLEX	0.701±0.128	0.624±0.154	0.462±0.191	1.869±0.803	1.056±0.239
	StNet	0.646±0.134	0.570±0.142	0.419±0.176	1.686±0.373	1.023±0.134
	BLEEP	0.637±0.112	0.556±0.120	0.382±0.160	2.038±0.587	1.096±0.164
	Stem	0.670±0.116	0.573±0.130	0.399±0.166	1.788±0.418	1.032±0.138
	HyperST	0.721±0.105	0.642±0.128	0.477±0.184	1.498±0.456	0.958±0.158
Skin	TRIPLEX	0.831±0.094	0.799±0.114	0.740±0.142	0.981±0.466	0.685±0.205
	StNet	0.804±0.105	0.779±0.117	0.726±0.140	0.993±0.469	0.689±0.198
	BLEEP	0.788±0.111	0.761±0.123	0.704±0.145	1.117±0.540	0.701±0.221
	Stem	0.782±0.094	0.748±0.113	0.687±0.138	1.276±0.703	0.730±0.261
	HyperST	0.839±0.086	0.812±0.102	0.758±0.129	0.932±0.418	0.657±0.182
Lung	TRIPLEX	0.567±0.247	0.499±0.272	0.393±0.272	1.537±1.307	0.849±0.446
	StNet	0.526±0.247	0.464±0.267	0.355±0.253	1.660±1.258	0.899±0.422
	BLEEP	0.488±0.212	0.412±0.235	0.311±0.230	1.803±1.507	0.891±0.465
	Stem	0.546±0.224	0.469±0.250	0.351±0.241	1.709±1.365	0.866±0.485
	HyperST	0.637±0.225	0.568±0.260	0.459±0.282	1.182±0.873	0.757±0.352

$$\mathcal{L}_{HEA} = \frac{1}{4}(\mathcal{L}_{entail}(\hat{I}_s, \hat{I}_n) + \mathcal{L}_{entail}(\hat{G}_s, \hat{G}_n) + \mathcal{L}_{entail}(\hat{I}_s, \hat{G}_s) + \mathcal{L}_{entail}(\hat{I}_n, \hat{G}_n)). \quad (10)$$

3.4. Gene Decoder Based on Aligned Representations and Objective Function

To predict the spot-level gene expression profiles, we directly concatenate the aligned representations (I_s and I_n) and feed the result into a gene decoder implemented by Multi-Layer Perceptron (MLP), which can be expressed by $Y^{pred} = Decoder_{gene}(\text{concat}(I_s, I_n))$. MSE loss is leveraged to optimize this decoder: $\mathcal{L}_{pred} = \|Y^{pred} - Y_s\|_2^2$.

The Training Objective Function The training objective of HyperST is twofold: (1) to align pathological images and gene expression profiles across multiple levels by modeling the hierarchical structure of ST data, and (2) to accurately predict gene expression from image features alone. This objective function consists of two components: hierarchical alignment loss and ST prediction loss, defined by:

$$\mathcal{L} = \mathcal{L}_{pred} + \alpha(\mathcal{L}_{HCA} + \beta\mathcal{L}_{HEA}), \quad (11)$$

where α balances the loss components, and β controls the entailment loss effect.

4. Experiments and Results

4.1. Experimental Settings

Dataset To evaluate HyperST, we collected four public datasets from the HEST-1K dataset [20], a high-quality collection of spatial transcriptomics data with standardized processing and rich metadata. (1) Kidney [23] provides 23 WSIs and 25,944 spots at a resolution of approximately 0.76 $\mu\text{m}/\text{pixel}$. (2) Colorectum dataset [41] comprises 14 WSIs (0.45 μm per pixel) with a total of 20,733 spots. (3) Skin [37] includes 46 WSIs and over 35,000 spots. The resolution of pathology images is about 0.52 $\mu\text{m}/\text{pixel}$. (4) Lung [28] consists of 16 WSIs at 0.45 $\mu\text{m}/\text{pixel}$ resolution and 31,445 spots. The spots of all datasets have a diameter of 55 μm .

ST Preprocessing To account for variations in image resolution across datasets, we adopted a physics-aware patch extraction strategy rather than using fixed pixel dimensions for image cropping. Specifically, we calculated the patch size for each spot based on its physical diameter and cropped the corresponding images at their respective resolutions to obtain spot-level image patches. The niche-level patch is created by cropping the region encompassing the central spot and its K-nearest neighbors (determined by spatial coordinates). Subsequently, all extracted patches are resized to a uniform 224×224 pixel resolution. For the gene expression data, we select the top 200 Highly Mean, Highly Variant Genes (HMHVG). Gene expression counts for each spot were subsequently log-transformed.

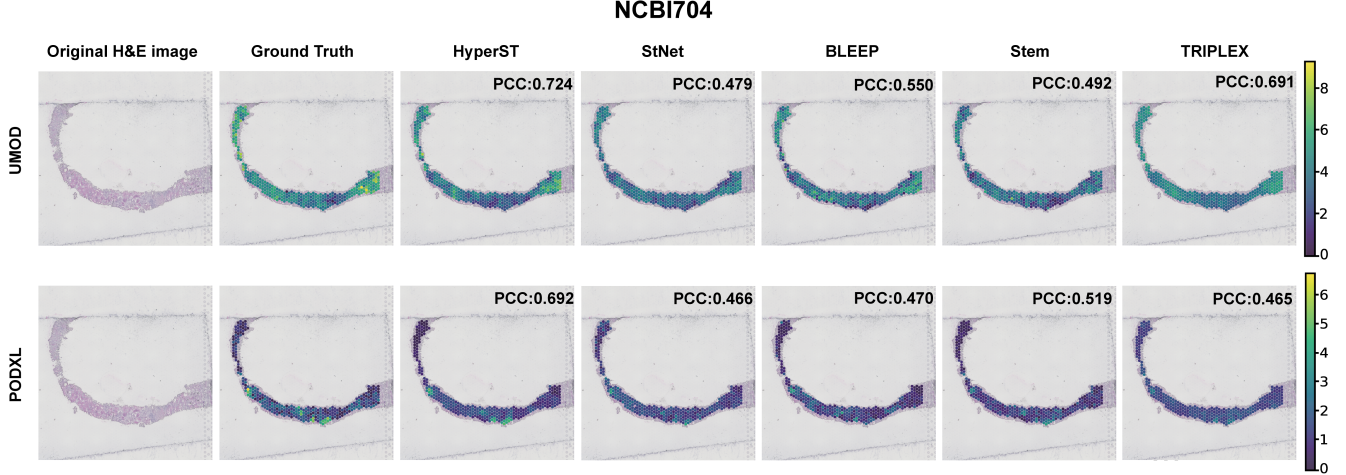


Figure 3. Visualization of the spatial distribution of the UMOD (Top) gene and PODXL gene (Bottom) in NCBI704 sample. The color scale ranges from purple/blue (low expression) to yellow/green (high expression).

Evaluation Protocol To ensure robust model evaluation, we performed five independent random splits of the WSI samples for each dataset, allocating 80% for training, 10% for validation, and 10% for testing in each iteration. The exact WSI IDs used for each of the five splits are provided in our code to ensure full reproducibility. Our evaluation metrics include top- k mean Pearson Correlation Coefficient ($PCC@k$), mean squared error (MSE), and mean absolute error (MAE), similar to [10, 50].

4.2. Experimental Results and Visualization

Baseline Comparison Table 1 shows that HyperST outperforms all existing methods across all datasets (Kidney, Colorectum, Skin and Lung), highlighting HyperST’s superior accuracy and robustness in predicting gene expression from pathology images across diverse biological contexts, which were trained under a rigorous, fair comparison protocol (details in the Section 7.2 of Supplementary Material). To emphasize the magnitude of this improvement, we compare HyperST to the second-best performing model, TRIPLEX. On the $PCC@200$ metric, HyperST demonstrates substantial relative improvements of approximately 10.95%, 3.24%, 2.52%, and 16.7% on the Kidney, Colorectum, Skin, and Lung datasets, respectively. Notably, while the next-best TRIPLEX confirms the value of multi-level features, it lacks explicit constraints for the intrinsic hierarchy. HyperST’s lead demonstrates the crucial advantage of our Hierarchical Hyperbolic Alignment.

Biomarker Visualization To further qualitatively assess the model’s behavior, we performed visualization of sample NCBI704 in the Kidney dataset, focusing on two established kidney cancer biomarkers, i.e., UMOD [40] and PODXL [2]. Figure 3 demonstrates that HyperST more accurately cap-

tures the key high-expression regions.

Table 2. Performance on MSI Status Classification (AUROC). Higher values on MSI-H and MSS are better.

Model	AUROC	
	MSI-H \uparrow	MSS \uparrow
TRIPLEX	0.630 \pm 0.048	0.567 \pm 0.032
StNet	0.571 \pm 0.080	0.541 \pm 0.029
BLEEP	0.550 \pm 0.045	0.530 \pm 0.056
Stem	0.584 \pm 0.078	0.544 \pm 0.034
HyperST	0.719\pm0.060	0.601\pm0.056

Clinical Downstream Task Validation We designed a downstream validation experiment to further validate the clinical utility of HyperST’s zero-shot gene expression predictions compared with other methods. First, we employed our model, pre-trained on the Colorectum dataset, to perform zero-shot inference on H&E slides from an independent external dataset, TCGA-COADREAD (colon and rectal adenocarcinoma). For each slide, HyperST predicts a gene expression vector for every spot. We then obtain a slide-level pseudo-bulk profile by averaging the predicted expression across all spots on that slide. The resulting pseudo-bulk profiles were then used to train a Random Forest classifier for predicting microsatellite instability (MSI) status, a critical clinical biomarker for immunotherapy response [12]. As shown in Table 2, the gene profiles predicted by HyperST led to significantly better MSI prediction performance compared to other baselines by capturing more clinically relevant signals. In this zero-shot setting, HyperST attains per-class AUROCs of 0.719 for MSI-H and 0.601 for MSS. Compared with the strongest baseline TRIPLEX (0.630 and 0.567, re-

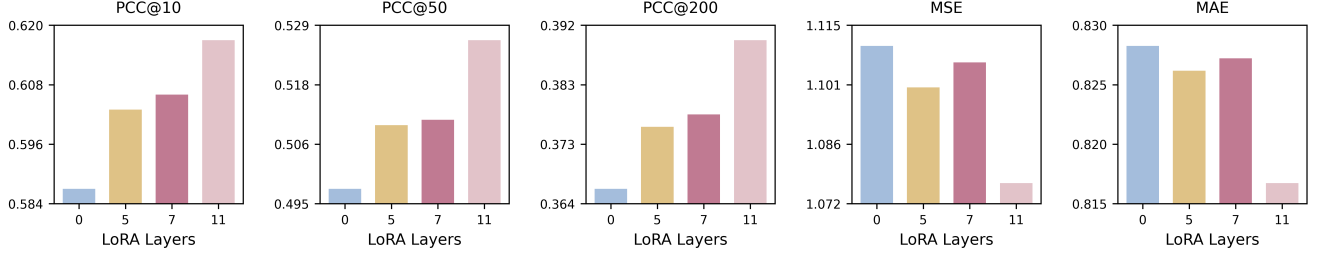


Figure 4. Result of ablation study on the choice of the last layers of LoRA.

Table 3. Ablation study of the alignment strategy.

Alignment	PCC@10 \uparrow	PCC@50 \uparrow	PCC@200 \uparrow	MSE \downarrow	MAE \downarrow
w/o G-I HEA	0.610 \pm 0.101	0.514 \pm 0.096	0.378 \pm 0.074	1.147 \pm 0.188	0.839 \pm 0.065
w/o HEA	0.603 \pm 0.092	0.508 \pm 0.083	0.368 \pm 0.061	1.112 \pm 0.185	0.831 \pm 0.065
w/o HEA + HCA	0.576 \pm 0.099	0.484 \pm 0.089	0.344 \pm 0.064	1.134 \pm 0.168	0.837 \pm 0.058
MERU	0.586 \pm 0.099	0.494 \pm 0.090	0.355 \pm 0.062	1.148 \pm 0.205	0.842 \pm 0.071
CLIP	0.558 \pm 0.098	0.462 \pm 0.087	0.321 \pm 0.058	1.220 \pm 0.293	0.867 \pm 0.097
Ours	0.617\pm0.094	0.526\pm0.088	0.390\pm0.070	1.077\pm0.155	0.817\pm0.058

spectively), HyperST achieves approximately 14% and 6% higher AUROC for MSI-H and MSS.

4.3. Ablation Study

We performed an ablation study on the model’s structure and hyperparameters to observe the strategy of alignment, input data for gene decoder and the impact of LoRA. Here, we describe the results on Kidney dataset.

Strategy of Alignment We compared the different alignment strategies including: a) removing only the gene-image regularization term of the HEA loss (w/o G-I HEA), b) removing the entire HEA loss (w/o HEA), c) removing the entire Hierarchical Hyperbolic Alignment (HHA) module (w/o HEA + HCA), d) replacing the HHA module by a MERU variant in Hyperbolic Space (without multi-level representation learning) [11] and e) replacing the HHA module by a CLIP variant in Euclidean Space [36]. As shown in Table 3, the results confirm our design. Removing the entire Hierarchical Hyperbolic Alignment module caused a 13.26% PCC@200 drop. Removing the entire HEA loss or just its gene-image regularization term led to 6.01% and 3.24% drops. Notably, the performance gap between our full model and its Euclidean counterpart (CLIP) strongly validates our core hypothesis on the superiority of hyperbolic space for this task.

Input of Decoder We evaluated the impact of different input strategies on the decoder’s performance, including using a) only spot-level image, b) only niche-level image and c) the combination of both. As shown in Table 4, the

results reveal that our combined approach yields the best performance across all metrics.

Table 4. Additional ablation study of the decoder input.

Decoder Input	PCC@200 \uparrow	MSE \downarrow	MAE \downarrow
only spot	0.353 \pm 0.067	1.171 \pm 0.184	0.849 \pm 0.065
only niche	0.356 \pm 0.073	1.110 \pm 0.139	0.828 \pm 0.051
spot+niche	0.390\pm0.070	1.077\pm0.155	0.817\pm0.058

Choice of LoRA During training, we found that increasing the number of the last attention layers in UNI adapted by LoRA modules improved performance. The corresponding evaluation results are shown in Figure 4. Our ablation study demonstrates that increasing LoRA layers from 0 to 11 layers generally improves predictive performance across most metrics. However, we observe marginal degradation in MSE and MAE when transitioning from 5 to 7 layers.

5. Conclusion

We present HyperST, a novel framework that leverages multi-level hyperbolic representations to predict spatial transcriptomics from histology images. By modeling the intrinsic hierarchical structure of ST data within hyperbolic space, HyperST learns more comprehensive spatial histological and genetic features. Our comprehensive experimental evaluation demonstrates that HyperST consistently outperforms state-of-the-art approaches, underscoring the potential of geometric deep learning in spatial omics analysis.

References

- [1] Jordan T Ash, Gregory Darnell, Daniel Munro, and Barbara E Engelhardt. Joint analysis of expression levels and histological images identifies genes associated with tissue morphology. *Nature communications*, 12(1):1609, 2021. 1
- [2] Moumita Barua, Eric Shieh, Johannes Schlondorff, Giulio Genovese, Bernard S Kaplan, and Martin R Pollak. Exome sequencing and in vitro studies identified podocalyxin as a candidate gene for focal and segmental glomerulosclerosis. *Kidney international*, 85(1):124–133, 2014. 7
- [3] James W Cannon, William J Floyd, Richard Kenyon, Walter R Parry, et al. Hyperbolic geometry. *Flavors of geometry*, 31(59-115):2, 1997. 3
- [4] Richard J Chen, Tong Ding, Ming Y Lu, Drew FK Williamson, Guillaume Jaume, Andrew H Song, Bowen Chen, Andrew Zhang, Daniel Shao, Muhammad Shaban, et al. Towards a general-purpose foundation model for computational pathology. *Nature Medicine*, 30(3):850–862, 2024. 1, 5
- [5] Wei-Ting Chen, Ashley Lu, Kathleen Craessaerts, Benjamin Pavie, Carlo Sala Frigerio, Nikky Corthout, Xiaoyan Qian, Jana Laláková, Malte Kühnemund, Iryna Voytyuk, et al. Spatial transcriptomics and in situ sequencing to study alzheimer’s disease. *Cell*, 182(4):976–991, 2020. 2
- [6] Ying Chen, Jiajing Xie, Yuxiang Lin, Yuhang Song, Wenxian Yang, and Rongshan Yu. Survmamba: State space model with multi-grained multi-modal interaction for survival prediction. *arXiv preprint arXiv:2404.08027*, 2024. 2
- [7] Ying Chen, Guoan Wang, Yuanfeng Ji, Yanjun Li, Jin Ye, Tianbin Li, Ming Hu, Rongshan Yu, Yu Qiao, and Junjun He. Slidechat: A large vision-language assistant for whole-slide pathology image understanding. In *Proceedings of the Computer Vision and Pattern Recognition Conference*, pages 5134–5143, 2025. 1
- [8] Seunghyuk Cho, Juyong Lee, Jaesik Park, and Dongwoo Kim. A rotated hyperbolic wrapped normal distribution for hierarchical representation learning. *NeurIPS*, 35:17831–17843, 2022. 3
- [9] Kyongho Choe, Unil Pak, Yu Pang, Wanjun Hao, and Xiuqin Yang. Advances and challenges in spatial transcriptomics for developmental biology. *Biomolecules*, 13(1):156, 2023. 2
- [10] Youngmin Chung, Ji Hun Ha, Kyeong Chan Im, and Joo Sang Lee. Accurate spatial gene expression prediction by integrating multi-resolution features. In *CVPR*, pages 11591–11600, 2024. 2, 5, 7
- [11] Karan Desai, Maximilian Nickel, Tanmay Rajpurohit, Justin Johnson, and Shanmukha Ramakrishna Vedantam. Hyperbolic image-text representations. In *International Conference on Machine Learning*, pages 7694–7731. PMLR, 2023. 2, 3, 4, 8
- [12] Yu Feng, Wenjuan Ma, Yupeng Zang, Yanying Guo, Young Li, Yixuan Zhang, Xuan Dong, Yi Liu, Xiaojuan Zhan, Zhizhong Pan, et al. Spatially organized tumor-stroma boundary determines the efficacy of immunotherapy in colorectal cancer patients. *Nature Communications*, 15(1):10259, 2024. 7
- [13] Masayuki Fujii, Shigeki Sekine, and Toshiro Sato. Decoding the basis of histological variation in human cancer. *Nature Reviews Cancer*, 24(2):141–158, 2024. 2
- [14] Octavian Ganea, Gary Bécigneul, and Thomas Hofmann. Hyperbolic entailment cones for learning hierarchical embeddings. In *International conference on machine learning*, pages 1646–1655. PMLR, 2018. 4
- [15] Songwei Ge, Shlok Mishra, Simon Kornblith, Chun-Liang Li, and David Jacobs. Hyperbolic contrastive learning for visual representations beyond objects. In *Proceedings of the IEEE/CVF conference on computer vision and pattern recognition*, pages 6840–6849, 2023. 2
- [16] Bryan He, Ludvig Bergenstråhle, Linnea Stenbeck, Abubakar Abid, Alma Andersson, Åke Borg, Jonas Maaskola, Joakim Lundberg, and James Zou. Integrating spatial gene expression and breast tumour morphology via deep learning. *Nature biomedical engineering*, 4(8):827–834, 2020. 2
- [17] Kaiming He, Xiangyu Zhang, Shaoqing Ren, and Jian Sun. Deep residual learning for image recognition. In *CVPR*, pages 770–778, 2016. 2
- [18] Joy Hsu, Jeffrey Gu, Gong Wu, Wah Chiu, and Serena Yeung. Capturing implicit hierarchical structure in 3d biomedical images with self-supervised hyperbolic representations. *NeurIPS*, 34:5112–5123, 2021. 2, 3
- [19] Edward J Hu, Yelong Shen, Phillip Wallis, Zeyuan Allen-Zhu, Yuanzhi Li, Shean Wang, Lu Wang, Weizhu Chen, et al. Lora: Low-rank adaptation of large language models. *ICLR*, 1(2):3, 2022. 5
- [20] Guillaume Jaume, Paul Doucet, Andrew H. Song, Ming Y. Lu, Cristina Almagro-Perez, Sophia J. Wagner, Anurag J. Vaidya, Richard J. Chen, Drew F. K. Williamson, Ahrong Kim, and Faisal Mahmood. Hest-1k: A dataset for spatial transcriptomics and histology image analysis. In *NeurIPS*, 2024. 6
- [21] Guillaume Jaume, Anurag Vaidya, Richard J Chen, Drew FK Williamson, Paul Pu Liang, and Faisal Mahmood. Modeling dense multimodal interactions between biological pathways and histology for survival prediction. In *CVPR*, pages 11579–11590, 2024. 2
- [22] Valentin Khulkov, Leyla Mirvakhabova, Evgeniya Ustinova, Ivan Oseledets, and Victor Lempitsky. Hyperbolic image embeddings. In *CVPR*, pages 6418–6428, 2020. 3
- [23] Blue B Lake, Rajasree Menon, Seth Winfree, Qiwen Hu, Ricardo Melo Ferreira, Kian Kalhor, Daria Barwinska, Edgar A Otto, Michael Ferkowicz, Dinh Diep, et al. An atlas of healthy and injured cell states and niches in the human kidney. *Nature*, 619(7970):585–594, 2023. 6
- [24] Hao Li, Ying Chen, Yifei Chen, Rongshan Yu, Wenxian Yang, Liansheng Wang, Bowen Ding, and Yuchen Han. Generalizable whole slide image classification with fine-grained visual-semantic interaction. In *CVPR*, pages 11398–11407, 2024. 1
- [25] Junnan Li, Ramprasaath Selvaraju, Akhilesh Gotmare, Shafiq Joty, Caiming Xiong, and Steven Chu Hong Hoi. Align before fuse: Vision and language representation learning with momentum distillation. *NeurIPS*, 34:9694–9705, 2021. 5
- [26] Yuxiang Lin, Ling Luo, Ying Chen, Xushi Zhang, Zihui Wang, Wenxian Yang, Mengsha Tong, and Rongshan Yu. St-align: A multimodal foundation model for image-gene alignment in spatial transcriptomics. *arXiv preprint arXiv:2411.16793*, 2024. 5

- [27] Ming Y Lu, Bowen Chen, Drew FK Williamson, Richard J Chen, Ivy Liang, Tong Ding, Guillaume Jaume, Igor Odintsov, Long Phi Le, Georg Gerber, et al. A visual-language foundation model for computational pathology. *Nature Medicine*, 30(3):863–874, 2024. 1
- [28] Elo Madissoon, Andrew J. Oliver, Viacheslav Kleshchevnikov, et al. A spatially resolved atlas of the human lung characterizes a gland-associated immune niche. *Nature genetics*, 55(1):66–77, 2023. 6
- [29] Pascal Mettes, Mina Ghadimi Atigh, Martin Keller-Ressel, Jeffrey Gu, and Serena Yeung. Hyperbolic deep learning in computer vision: A survey. *IJCV*, 132(9):3484–3508, 2024. 3
- [30] Taku Monjo, Masaru Koido, Sato Nagasawa, Yutaka Suzuki, and Yoichiro Kamatani. Efficient prediction of a spatial transcriptomics profile better characterizes breast cancer tissue sections without costly experimentation. *Scientific reports*, 12(1):4133, 2022. 2
- [31] Maximilian Nickel and Douwe Kiela. Learning continuous hierarchies in the lorentz model of hyperbolic geometry. In *International conference on machine learning*, pages 3779–3788. PMLR, 2018. 3
- [32] Ajit J Nirmal, Zoltan Maliga, Tuulia Vallius, Brian Quatrochi, Alyce A Chen, Connor A Jacobson, Roxanne J Pelletier, Clarence Yapp, Raquel Arias-Camison, Yu-An Chen, et al. The spatial landscape of progression and immunoediting in primary melanoma at single-cell resolution. *Cancer discovery*, 12(6):1518–1541, 2022. 2
- [33] Aaron van den Oord, Yazhe Li, and Oriol Vinyals. Representation learning with contrastive predictive coding. *arXiv preprint arXiv:1807.03748*, 2018. 5
- [34] Avik Pal, Max van Spengler, Guido Maria D’Amely di Melendugno, Alessandro Flaborea, Fabio Galasso, and Pascal Mettes. Compositional entailment learning for hyperbolic vision-language models. *arXiv preprint arXiv:2410.06912*, 2024. 3
- [35] Marija Pizurica, Yuanning Zheng, Francisco Carrillo-Perez, Humaira Noor, Wei Yao, Christian Wohlfart, Antoaneta Vladimirova, Kathleen Marchal, and Olivier Gevaert. Digital profiling of gene expression from histology images with linearized attention. *Nature Communications*, 15(1):9886, 2024. 2
- [36] Alec Radford, Jong Wook Kim, Chris Hallacy, Aditya Ramesh, Gabriel Goh, Sandhini Agarwal, Girish Sastry, Amanda Askell, Pamela Mishkin, Jack Clark, et al. Learning transferable visual models from natural language supervision. In *International conference on machine learning*, pages 8748–8763. PmLR, 2021. 3, 8
- [37] Alexander Schäbitz, C Hillig, M Mubarak, Manja Jargosch, Ali Farnoud, Emanuele Scala, Nils Kurzen, Anna Caroline Pilz, Nayanika Bhalla, Jenny Thomas, et al. Spatial transcriptomics landscape of lesions from non-communicable inflammatory skin diseases. *Nature Communications*, 13(1):7729, 2022. 6
- [38] Patrik L Ståhl, Fredrik Salmén, Sanja Vickovic, Anna Lundmark, José Fernández Navarro, Jens Magnusson, Stefania Giacomello, Michaela Asp, Jakub O Westholm, Mikael Huss, et al. Visualization and analysis of gene expression in tissue sections by spatial transcriptomics. *Science*, 353(6294):78–82, 2016. 1
- [39] Zhonghui Tang, Yinqi Bai, Qi Fang, Yuchen Yuan, Qianwen Zeng, Shuling Chen, Tianyi Xu, Jianyu Chen, Li Tan, Chunqing Wang, et al. Spatial transcriptomics reveals tryptophan metabolism restricting maturation of intratumoral tertiary lymphoid structures. *Cancer Cell*, 2025. 2
- [40] Michael Turner and Natalie Staplin. Umodulating ckd risk: untangling the relationship between urinary uromodulin, blood pressure, and kidney disease. *Kidney international*, 100(6):1168–1170, 2021. 7
- [41] Alberto Valdeolivas, Bettina Amberg, Nicolas Giroud, Marion Richardson, Eric JC Gálvez, Solveig Badillo, Alice Julien-Laferrière, Demeter Túrós, Lena Voith von Voithenberg, Isabelle Wells, et al. Profiling the heterogeneity of colorectal cancer consensus molecular subtypes using spatial transcriptomics. *NPJ precision oncology*, 8(1):10, 2024. 6
- [42] Chuhan Wang, Adam S Chan, Xiaohang Fu, Shila Ghazanfar, Jinman Kim, Ellis Patrick, and Jean YH Yang. Benchmarking the translational potential of spatial gene expression prediction from histology. *Nature Communications*, 16(1):1544, 2025. 2
- [43] Hongyi Wang, Xiuju Du, Jing Liu, Shuyi Ouyang, Yen-Wei Chen, and Lanfen Lin. M2ost: Many-to-one regression for predicting spatial transcriptomics from digital pathology images. In *AAAI*, pages 7709–7717, 2025. 2
- [44] Cameron G Williams, Hyun Jae Lee, Takahiro Asatsuma, Roser Vento-Tormo, and Ashraf Haque. An introduction to spatial transcriptomics for biomedical research. *Genome medicine*, 14(1):68, 2022. 2
- [45] Sijia Wu, Jiajin Zhang, Yanfei Wang, Xinyu Qin, Zhaocan Zhang, Zhennan Lu, Pora Kim, Xiaobo Zhou, and Liyu Huang. metsdb: a knowledgebase of cancer metastasis at bulk, single-cell and spatial levels. *Nucleic Acids Research*, 53(D1):D1427–D1434, 2025. 2
- [46] Ronald Xie, Kuan Pang, Sai Chung, Catia Perciani, Sonya MacParland, Bo Wang, and Gary Bader. Spatially resolved gene expression prediction from histology images via bimodal contrastive learning. *NeurIPS*, 36:70626–70637, 2023. 2, 3, 4, 5
- [47] Jiazhou Ye, Yan Lin, Zhiling Liao, Xing Gao, Cheng Lu, Lu Lu, Julu Huang, Xi Huang, Shilin Huang, Hongping Yu, et al. Single cell-spatial transcriptomics and bulk multi-omics analysis of heterogeneity and ecosystems in hepatocellular carcinoma. *NPJ Precision Oncology*, 8(1):262, 2024. 2
- [48] Linlin Zhang, Dongsheng Chen, Dongli Song, Xiaoxia Liu, Yanan Zhang, Xun Xu, and Xiangdong Wang. Clinical and translational values of spatial transcriptomics. *Signal Transduction and Targeted Therapy*, 7(1):111, 2022. 2
- [49] Yikun Zhang, Geyan Ye, Chaohao Yuan, Bo Han, Long-Kai Huang, Jianhua Yao, Wei Liu, and Yu Rong. Atomas: Hierarchical adaptive alignment on molecule-text for unified molecule understanding and generation. In *ICLR*, 2025. 5
- [50] Sichen Zhu, Yuchen Zhu, Molei Tao, and Peng Qiu. Diffusion generative modeling for spatially resolved gene expression inference from histology images. *arXiv preprint arXiv:2501.15598*, 2025. 2, 4, 7